

Supplementary Material for
“Quasiparticle Interference, quasiparticle interactions and the
origin of the charge density-wave in 2H-NbSe₂”

C. J. Arguello¹, E. P. Rosenthal¹, E. F. Andrade¹, W. Jin², P. C. Yeh², N. Zaki³, S. Jia⁴, R. J. Cava⁴, R. M. Fernandes⁵, A. J. Millis¹, T. Valla⁶, R. M. Osgood Jr.^{2,3}, A. N. Pasupathy¹

1. Department of Physics, Columbia University, NY, NY, 10027

*2. Department of Applied Physics and Applied Math,
Columbia University, NY, NY, 10027*

*3. Department of Electrical Engineering,
Columbia University, NY, NY, 10027*

4. Department of Chemistry, Princeton University, Princeton NJ 08540

*5. School of Physics and Astronomy,
University of Minnesota, Minneapolis, MN 55455*

6. Brookhaven National Laboratory, Upton, NY 11973

(Dated: November 6, 2014)

I. RELATING THE CHARGE SUSCEPTIBILITY AND QPI

Here we present specifics of the relation between the measured QPI intensity and basic electronic properties including the bare charge susceptibility.

A. Derivation of Eq. 3 of main text

We start from the basic tunneling Hamiltonian connecting the tunneling tip to a state of the system of interest:

$$H_{\text{tun}} = \int d^3\mathbf{r} V_{\text{tun}}(\mathbf{r}) \psi_{\text{tip}}^\dagger \psi_{\text{system}}(\mathbf{r}) + H.c. \quad (1)$$

Expressing the system operator at position \mathbf{r} in terms of the operators $\psi_{n\mathbf{p}}$ that annihilate electrons in band state n and momentum \mathbf{p} in the first Brillouin zone as

$$\psi_{\text{system}}(\mathbf{r}) = \sum_{n\mathbf{p}} u_{n\mathbf{p}}(\mathbf{r}) e^{-i\mathbf{p}\cdot\mathbf{r}} \psi_{n\mathbf{p}}, \quad (2)$$

performing the usual second order perturbative analysis of the tunneling transition rate and differentiating with respect to the voltage difference between tip and sample gives

$$\frac{dI}{dV}(\mathbf{r}; E) = \sum_{mn;\mathbf{p}\mathbf{q}} |V_{\text{tun}}(\mathbf{r})|^2 u_{n\mathbf{p}}^*(\mathbf{r}) u_{m\mathbf{q}}(\mathbf{r}) e^{i\mathbf{r}\cdot(\mathbf{p}-\mathbf{q})} \frac{G_{nm}(\mathbf{p}, \mathbf{q}; E - i\delta) - G_{nm}(\mathbf{p}, \mathbf{q}; E + i\delta)}{2\pi i} \quad (3)$$

Writing a position \mathbf{r} in unit cell j (central position \mathbf{R}_j) as $\mathbf{r} = \mathbf{R}_j + \boldsymbol{\xi}$ and averaging over the in-unit cell coordinate $\boldsymbol{\xi}$ gives

$$\frac{dI}{dV}(j; E) = \sum_{mn;\mathbf{p}\mathbf{q}} M_{mn;\mathbf{p}\mathbf{q}}^{\text{tun}} e^{i\mathbf{R}_j\cdot(\mathbf{p}-\mathbf{q})} \frac{G_{nm}(\mathbf{p}, \mathbf{q}; E - i\delta) - G_{nm}(\mathbf{p}, \mathbf{q}; E + i\delta)}{2\pi i} \quad (4)$$

with

$$M_{mn;\mathbf{p}\mathbf{q}}^{\text{tun}} = \int_{\text{unit cell}} d^3\boldsymbol{\xi} |V_{\text{tun}}(\boldsymbol{\xi})|^2 u_{n\mathbf{p}}^*(\boldsymbol{\xi}) u_{m\mathbf{q}}(\boldsymbol{\xi}) e^{i\boldsymbol{\xi}\cdot(\mathbf{p}-\mathbf{q})} \quad (5)$$

Finally assuming that the combination of the tunneling matrix element and the atomic wave functions has no interesting spatial structure (\mathbf{M} independent of \mathbf{p}, \mathbf{q}) and evaluating the momentum sums in Eq. 4 gives

$$\frac{dI}{dV}(\mathbf{R}; E) = \sum_{mn} M_{mn}^{\text{tun}} \frac{G_{nm}(\mathbf{R}, \mathbf{R}; E - i\delta) - G_{nm}(\mathbf{R}, \mathbf{R}; E + i\delta)}{2\pi i} \quad (6)$$

which is Eq. (1) of the main text.

B. Relation between QPI and Lindhard function

The static Lindhard or particle-hole bubble susceptibility representing transitions between bands n and m , $\chi^{mn}(k, \nu = 0)$ may be written

$$\chi(\mathbf{k}) = -T \sum_{\omega_n, \mathbf{p}} (G^n(\mathbf{p}, \omega_n) G^m(\mathbf{p} + \mathbf{k}, \omega_n) + G^m(\mathbf{p}, \omega_n) G^n(\mathbf{p} + \mathbf{k}, \omega_n)) \quad (7)$$

Evaluating the sum in the usual way by converting to a contour integral in the complex plane which is evaluated in terms of the discontinuity across the branch cut along the real axis gives Eq. 7 of the main text.

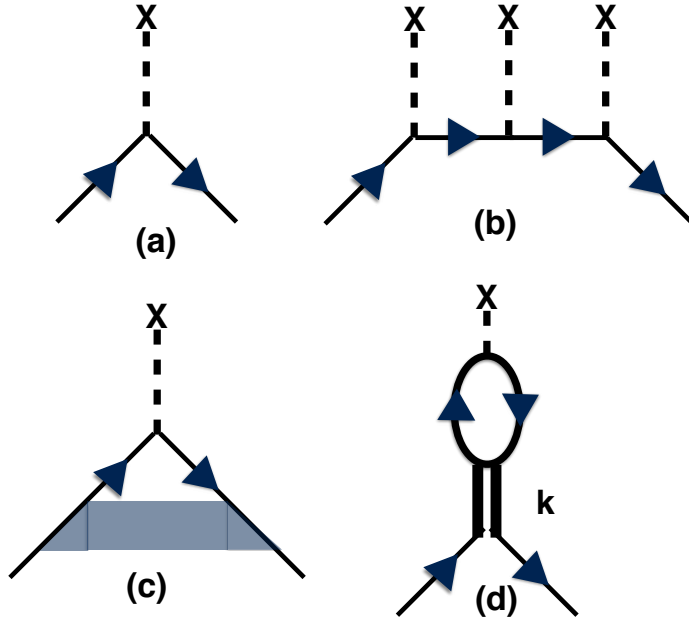


FIG. 1. Diagrammatic representation of electron impurity scattering. (a) single scattering event; (b) example of multiple scattering from an impurity; sum of all such diagrams yield the bare T-matrix; (c) single scattering event renormalized by general electron-electron interaction vertex (d) single scattering event renormalized by phonon. Dashed line with **X**: bare electron-impurity vertex; solid line with arrow: electron propagator as determined from ARPES (i.e. renormalized by self energy); shaded box: general vertex correction; heavy double line: phonon propagator with phonon momentum \mathbf{k} indicated.

C. Interactions and the T-matrix

The basic electron-impurity vertex is shown diagrammatically in Fig. 1a. Multiple scattering off of the impurity is shown diagrammatically in Fig. 1(b). A general vertex corrections (interaction of the incoming and outgoing electron) is shown in panel Fig. 1(c). The particular case of an electron-phonon renormalization is shown in Fig. 1(d).

II. TIGHT BINDING FIT TO ARPES DATA

Energy distribution curves (EDCs) and momentum distribution curves (MDCs) for the ARPES spectra are shown in Fig. 2(a) and Fig. 2 (b), respectively. Quasiparticle dispersions are obtained from fits to peak positions, which in turn are determined by fitting the measured EDCs and MDCs to a sum of gaussians, a linear background, and a Fermi function. For example, in Fig. 2 (c), the EDC data (black dots) are fitted with two Gaussians (blue dashed curves), a linear background, and a Fermi function; in Fig. 2 (d), the MDC data (black dots) are fitted with four Gaussians (blue dashed curves) and a linear background. The energy and momentum positions of the peaks are shown in Fig. 3 as empty circles.

We fit these two bands to a previously-proposed [1] five-nearest-neighbor tight-binding model to extract the band dispersions (red solid curves). The bands of the tight-binding model are given by the following expression:

$$\begin{aligned}
 E_i(k_x, k_y) = & t_{0,i} + t_{1,i}(2 \cos(\eta_x) \cos(\eta_y) + \cos(2\eta_x)) \\
 & + t_{2,i}(2 \cos(3\eta_x) \cos(\eta_y) + \cos(2\eta_y)) \\
 & + t_{3,i}(2 \cos(2\eta_x) \cos(2\eta_y) + \cos(4\eta_x)) \\
 & + t_{4,i}(\cos(\eta_x) \cos(3\eta_y) + \cos(5\eta_x) \cos(\eta_y) \\
 & + \cos(4\eta_x) \cos(2\eta_y))
 \end{aligned} \tag{8}$$

with

$$\eta_x = \frac{1}{2}k_x a \quad \eta_y = \frac{\sqrt{3}}{2}k_y a \tag{9}$$

These expressions model the quasi two-dimensional Nb-derived bands that are observed in ARPES experiments. A Se-derived band with strong k_z dispersion is also found in DFT calculations [2] but is typically not seen in ARPES[3]. The strong k_z dispersion of this

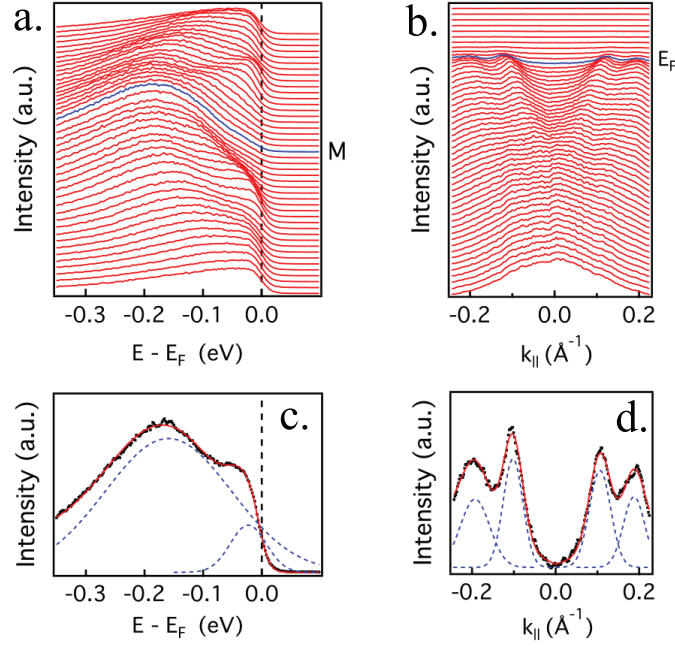


FIG. 2. (a) Energy distribution curve (EDCs) and (b) Momentum distribution curves (MDCs) for the ARPES spectra shown in Fig. 2 (a). (c) EDC and (d) MDC are fitted to determine the peak positions. Black dots denote the experimental data, red solid curves represent the fit curves, and blue dashed curves are Gaussians.

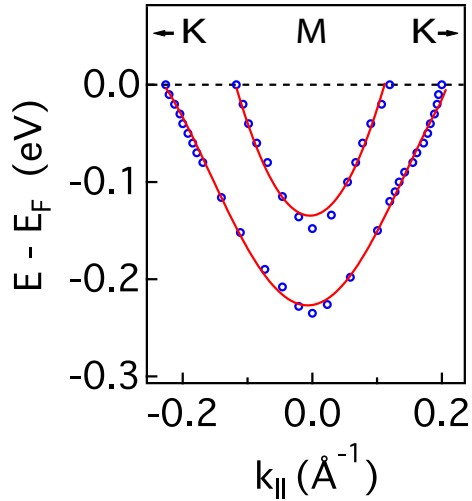


FIG. 3. Tight binding fit to the band dispersion. Blue empty circles denote the peak positions extracted from the EDC and MDC fitting shown in Fig. 2. Red solid curves are tight-binding fits.

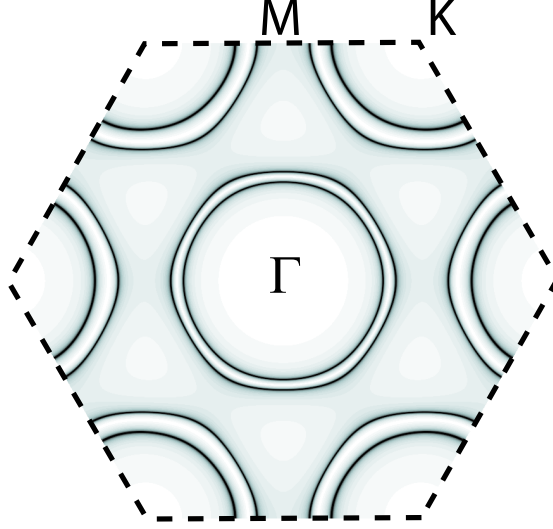


FIG. 4. Fermi Surface calculated from the Tight Binding fit to the ARPES data.

band also means that it will contribute less to the QPI. We do not consider it here. The parameters of the model are given in Table I.

Parameter (meV)	t_0	t_1	t_2	t_3	t_4
Band 1	14.2	82.8	255.4	42.9	20.5
Band 2	265	21.0	407.2	8.8	-1.0

TABLE I. Tight binding parameters from ARPES. Note that in these conventions the Fermi energy is set to 0.

From the tight binding parameters we calculate the components of B via the computationally efficient expression [2]:

$$B^{nm}(\mathbf{k}, E) = \int_{-\infty}^0 d\alpha \int_0^{\infty} \frac{d\beta}{\alpha - \beta} F_{nm}(\alpha, \beta, \mathbf{k}) \quad (10)$$

$$F_{nm}(\alpha, \beta, \mathbf{k}) = \int \frac{d\mathbf{k}'}{(2\pi)^2} [\delta(E_n(\mathbf{k}') - \alpha) \delta(E_m(\mathbf{k}' + \mathbf{k}) - \beta)] \quad (11)$$

III. PARTIAL SUSCEPTIBILITY CALCULATED FROM STS

Proceeding from Eq. 5 of the main text we observe that if the T matrix has negligible energy dependence and couples all bands equally then the integral of the measured QPI

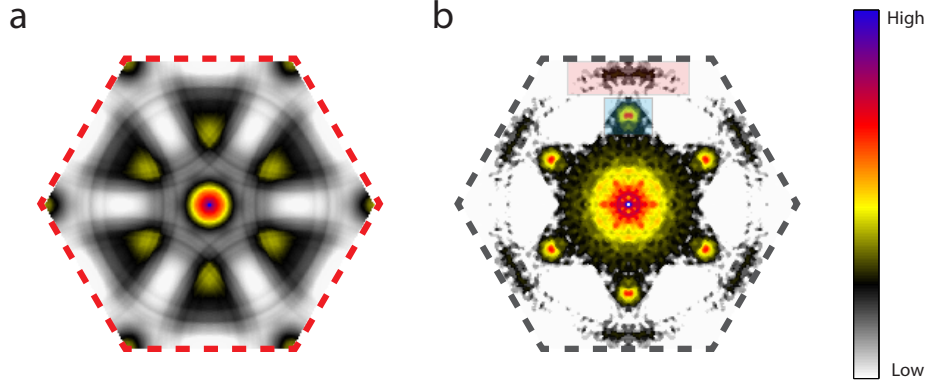


FIG. 5. Comparison of the electronic susceptibility calculated from ARPES (panel (a), $\sum_{mn} \chi^{mn}$ with χ from Eq. 7 of main text and B^{mn} from Eqs. 10,11) and from the STS data (panel (b), Eq. 12).

signal over a range from $-E_0$ (chosen such that $E_0 \gg kT$) to the Fermi level is, up to a constant, just an approximation χ_0 to the sum of all components of the static susceptibility χ :

$$\int_{-E_0}^0 dE f(E) \left| \delta \frac{dI(\mathbf{k}, E)}{dV} \right| \propto T(\mathbf{k}) \sum_{nm} \int_{-E_0}^0 dE f(E) B^{nm}(\mathbf{k}, E) = T(\mathbf{k}) \chi_0(\mathbf{k}) \approx T(\mathbf{k}) \chi(\mathbf{k}) \quad (12)$$

At the temperatures of the experiment (27 K), the Fermi function can be replaced with a step function, and the integral of the dI/dV signal from $-E_0$ to 0 is simply the experimentally measured current $I(-E_0)$. We choose a cutoff $E_0 = 150 \text{ meV} \gg kT = 2.5 \text{ meV}$, and plot the experimentally measured $I(-150 \text{ mV})$ in figure 5, where the portion of the signal coming from the CDW is highlighted with the blue rectangle while the dispersing QPI signal is indicated by the red rectangle. Also shown in Figure 5 is the calculated $\chi(\mathbf{k})$ obtained from Eq. 7 of the text using the B as computed from the ARPES bands as in Eqs. 10 and 11. The broad peaks in the χ calculated from ARPES (Fig. 5 (a)) are located at $k \simeq 0.74 k_{CDW}$ as has noted before [4]. The clear disagreement between the two figures points to the key role played by the momentum dependence of the T-matrix in enhancing certain scattering wave vectors in the observed QPI.

IV. REAL SPACE dI/dV MAPS

We present here a sequence of dI/dV measurements for different energies.

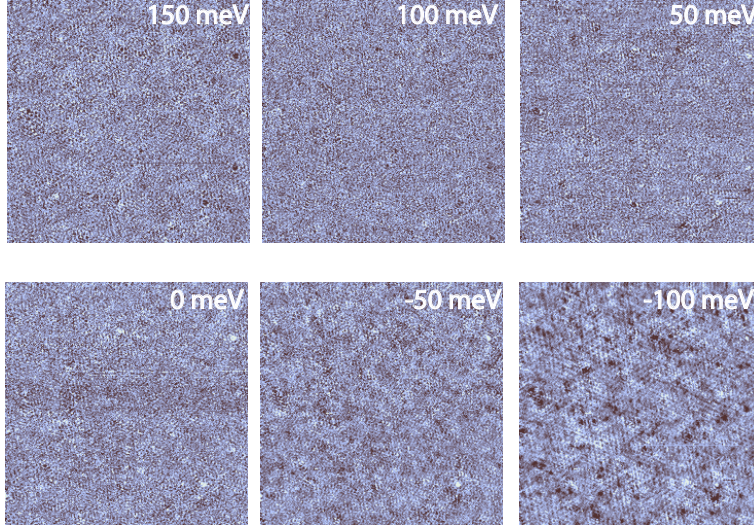


FIG. 6. dI/dV maps for different energies used in the main text

V. COMPARISON BETWEEN FT-STIS AND ARPES B

In Figure 7 we present an expanded view of the comparison between the Fourier transform of the measured STS data and the B calculated from ARPES at energies ranging from well below the Fermi level to well above. We zoom in a particular region of k -space that shows dispersing features. The left half of each subfigure is the FT-STIS data while the right half is the calculated B . The dispersing QPI feature is located along the $\Gamma - M$ direction at wavevectors larger than k_{CDW} . Zooming in to the region of k -space where QPI is observed, we see from Figure 7 that the FT-STIS signal is located near the edge of the Brillouin zone at energies well below E_F , and disperses steadily inwards at higher energies. Within this restricted region of k -space, the dispersion of the FT-STIS data matches very well with the B calculated from ARPES at all energies.

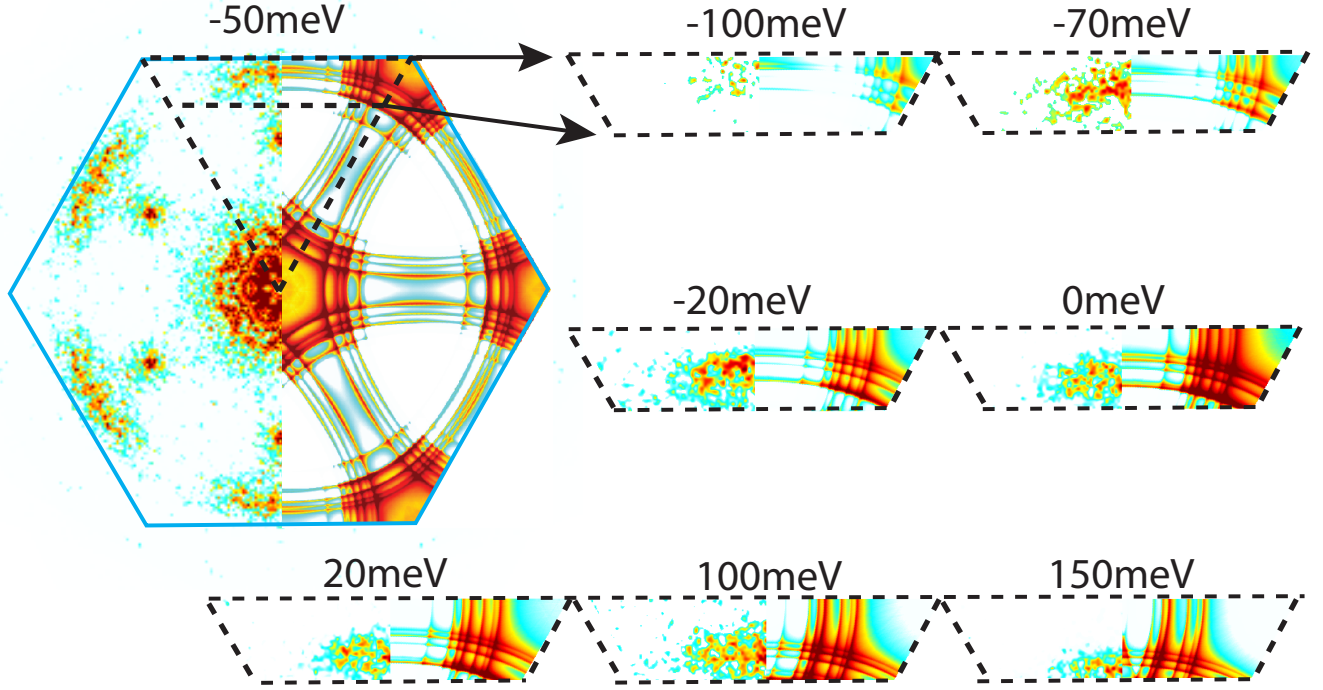


FIG. 7. Comparison between FT-STs and B calculated from ARPES at energies indicated. Shown for each energy is a slice of k -space from the Brillouin zone boundary near the M point, inwards to a wave vector somewhat larger than the CDW wave vector. The left half of each subfigure is the FT-STs data while the right half is the calculated B . Within the restricted region of k -space shown, the dispersion of the FT-STs data matches very well with the B calculated from ARPES at all energies.

VI. CDW WAVELENGTH VERSUS ENERGY

In this section we present a quantitative analysis of the location of the CDW peak in Fourier space at different energies. In order to locate the CDW peak, a line-cut along the CDW wavevector was fitted to a function $f(k)$ (Eq. 13) containing two gaussians corresponding to the CDW + QPI signals, and an extra exponentially decaying term which subtracts the small wavelength background noise from the signal.

$$f(k) = A_1 e^{-b_1 k} + A_2 e^{-b_2 (k-c_1)^2} + A_3 e^{-b_3 (k-c_2)^2} \quad (13)$$

$A_1, A_2, A_3, b_1, b_2, b_3, c_1, c_2$ are fitting parameters. The location of the CDW peak is given by the center of the first gaussian term (c_1). An example of the fitting and the results of the position of the CDW peak for all the studied energies are shown in figure 8. We conclude

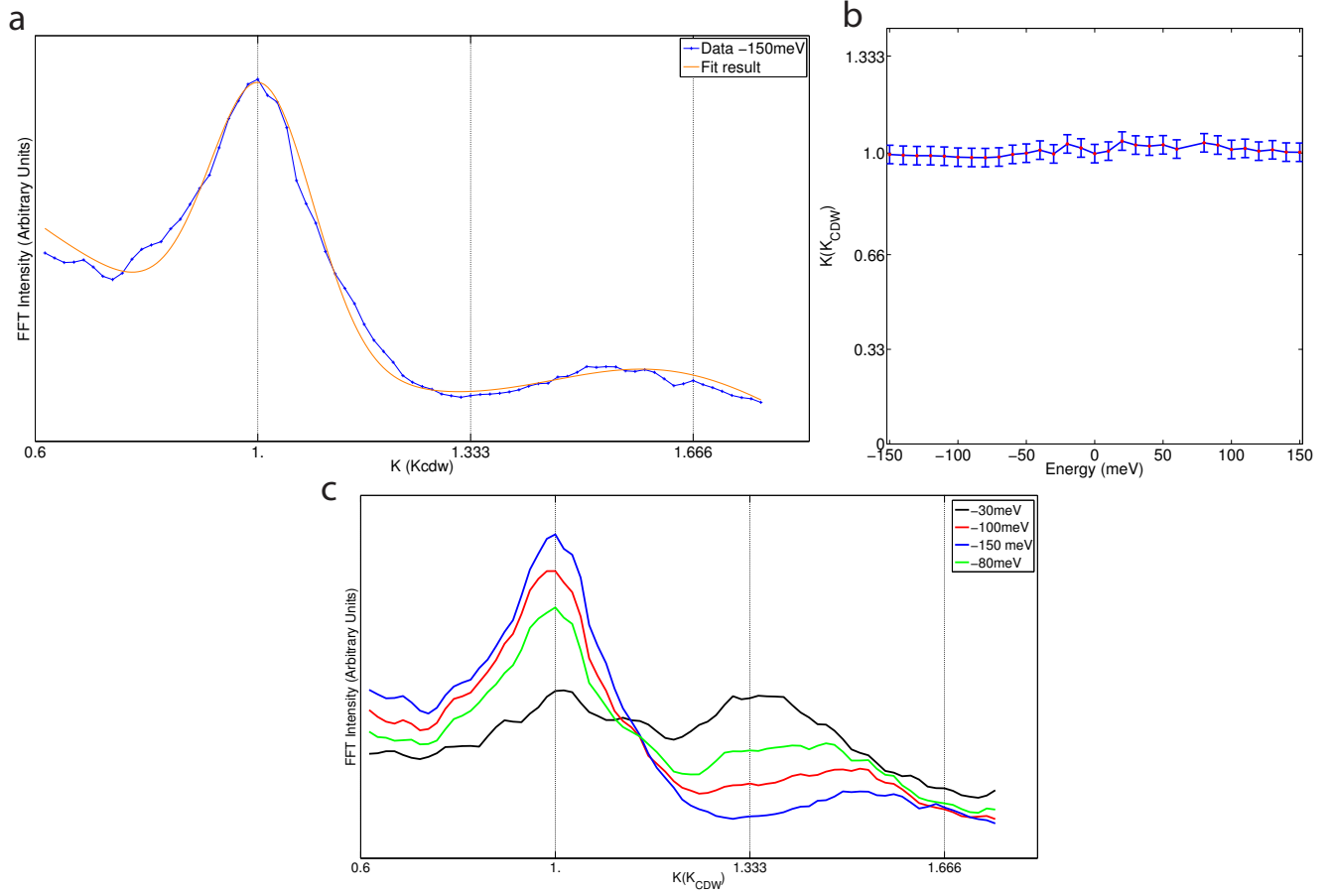


FIG. 8. a. Example of the fitting for $E = -150$ meV, locating the CDW peak. The line-cut of the data is in blue and the result of the fit is in orange. b. CDW peak position as a function of energy for the complete dataset. The dashed lines show the maximum/minimum K possible value of the feature associated with the CDW. c. Line-cuts for 4 different energies. The CDW peak position remains static.

that the CDW peak is a static feature (not dispersing with energy) within our experimental resolution.

-
- [1] D. J. Rahn, S. Hellmann, M. Kalläne, C. Sohrt, T. K. Kim, L. Kipp and K. Rossnagel, Phys. Rev. B **85** 224532 (2012).
- [2] M. D. Johannes, I. I. Mazin, and C. A. Howells, Phys. Rev. B **73**, 205102 (2006).
- [3] T. Kiss, T. Yokoya, A. Chainani, S. Shin, T. Hanaguri, M. Nohara and H. Takagi. Nat. Phys. **3**, 720 (2007).
- [4] D. S. Inosov, V. B. Zabolotnyy, D. V. Evtushinsky, A. A. Kordyuk, B. Buchner, R. Follath, H. Berger and S. V. Borisenko. New Journal of Physics **10**, 125027 (2008).